The Microstructure and Mechanical Properties of 3D Printed Carbon Nanotube-Polylactic Acid Composites

Huseini S. Patanwala,[1] **Danting Hong**,[2] **Sahil R. Vora**,[2] **Brice Bognet**,[1] **Anson W. K. Ma**[1,2]
[1]*Polymer Program, Institute of Materials Science, University of Connecticut, Storrs 06269, Connecticut*

[2]*Department of Chemical and Biomolecular Engineering, University of Connecticut, Storrs 06269, Connecticut*

This article reports 3D printing of carbon nanotube-polylactic acid (CNT-PLA) composites using an extrusion-based Fused Deposition Modeling (FDM) method. CNTs with an average diameter of 128 nm and an average length of 2.5 μm were first compounded with PLA and extruded into feedstock filaments at 0.5%, 2.5%, and 5% (w/w) CNT loadings. CNT aggregates were observed, but no clogging occurred during printing with a 500-μm print nozzle. The rheology of the CNT-PLA samples was characterized to understand the printing-induced alignment of CNTs along the road axis. Additionally, the effect of printing flow rate was explored for a fixed printing gap and nozzle diameter. Higher flow rates reduced the void fraction in the FDM parts, but unexpectedly resulted in less degree of CNT alignment, which is attributed to radial flow and fusion between adjacent roads. The mechanical properties of the CNT-PLA tensile test coupons were characterized. Inclusion of CNTs increased the Young's modulus by 30% at 5% CNT loading, but reduced the tensile strength and overall toughness of the FDM parts. Experimental data were compared against the Rule of Mixtures (RoM) model, the Halpin-Tsai model, and the modified RoM model and were further explained by the void fraction and CNT orientation. POLYM. COMPOS., 00:000–000, 2017. © **2017 Society of Plastics Engineers**

INTRODUCTION

3D printing is an additive manufacturing technique, wherein three-dimensional objects are created layer-by-layer or drop-by-drop with minimal material waste. 3D printing is capable of creating complex, highly customized, and net-shaped structures that are otherwise difficult or impossible to produce using conventional methods such as injection molding [1, 2]. Fused Deposition Modeling (FDM) is one of the most common methods used for 3D printing. It is based on micro-extrusion of thermoplastic polymers in a raster pattern through a nozzle. For better processibility, most FDM methods use thermoplastics, such as polylactic acid (PLA) and acrylonitrile butadiene styrene (ABS), with a low glass transition temperature (<100°C). FDM parts are great for rapid prototyping purposes but lack the physical properties for practical applications. There are two general approaches to improve the properties of FDM parts, namely, by choosing polymers with better properties (e.g., polyaryletherketone [3] and liquid crystalline polymers [4]) and by incorporating fillers in the neat polymers [5, 6]. Identifying appropriate polymer grades and developing new formulations for 3D printing constitute an active area of research.

This paper explores carbon nanotubes (CNTs) as short fiber fillers to improve the thermal and mechanical properties of PLA-based FDM parts. PLA is widely utilized in FDM because of its thermal properties and ease of use during printing. PLA degrades into lactic acid and further into carbon dioxide and water through hydrolysis making it a useful material for creating biodegradable scaffolds for biomedical applications [7]. PLA has a low glass transition temperature (T_g) of 55–65°C, which also coincides with the heat deflection temperature (HDT) of most PLA resins. Improving HDT of PLA requires achieving a maximum crystalline content of about 38% [8], which is undesirable from the processing perspective, as crystallinity tends to cause shrinkage and warpage in FDM processes. Further improvement in HDT can be achieved with the addition of fillers. However, care must be taken in choosing the filler material as fillers can act as a nucleating agent which results in an increase in PLA crystallinity.

In this study, CNT is chosen as the reinforcement material because of their excellent intrinsic mechanical, thermal, and electrical properties [9–11]. Further, CNT is

Additional Supporting Information may be found in the online version of this article.

Correspondence to: A. W. K. Ma; e-mail:anson.ma@uconn.edu

Contract grant sponsor: GE graduate fellowship.
A part of this work was presented at the 2015 Materials Research Society Fall Meeting held in Boston, MA.
DOI 10.1002/pc.24494
Published online in Wiley Online Library (wileyonlinelibrary.com).

available in powder form, allowing for direct blending into PLA and extrusion into feedstock filaments for the FDM printer. This process is different from continuous fiber composites printing which requires a specialized printer and carefully chosen polymers (e.g., MarkForged) [12, 13]. A number of studies exist on including fillers in neat polymers for 3D printing. Tekinalp et al. 3D printed carbon fiber–ABS composites and compared the mechanical properties to samples processed by compression molding [14]. Samples prepared by these two methods exhibited comparable tensile strength and modulus, although fiber orientation, dispersion, and void formation were different. Carbon fiber loading of as high as 40 wt% was compounded with neat ABS but could not be successfully 3D printed. Extrudate or printed filaments are referred to as "roads," and porosity between the roads is a typical feature of FDM parts. In addition to inter-road porosity, Tekinalp et al. observed additional void between the fillers and the polymer matrix in the printed composites at high filler loadings. Nozzle clogging is another major challenge that needs to be overcome while printing with high fiber loading. This challenge can be partially addressed by using a large diameter (>500 μm) nozzle, but the lateral resolution of the print will be compromised as a result. Shofner et al. 3D printed vapor grown carbon fiber–ABS composites and increased the average tensile strength and Young's modulus by 39% and 60%, respectively [15]. Compton et al. incorporated nano-clay platelets in a thermally curable epoxy and observed high anisotropy upon printing, which helps improve the Young's modulus in the load bearing direction [16].

Compared to more conventional processing methods like injection molding, structure-processing-properties relations in 3D printing are not well established. Many studies attempted to optimize the mechanical parts by varying process parameters, such as, deposition speed, nozzle temperature, the gap between the print nozzle and build plate, infill pattern, infill density, and part slicing layer thickness [17, 18]. This study is limited to exploring the effects of printing flow rate and CNT concentration on the structure and subsequent properties of FDM parts. Mechanical properties are benchmarked against existing literature data on PLA-CNT composites and explained in terms of preferential alignment of CNTs induced during 3D printing.

EXPERIMENTAL

Materials

CNTs used in this study are multiwalled CNTs produced using the chemical vapor deposition method. They were purchased from Sigma Aldrich (Cat# 65,9258, Lot# MKBG9911V) and used without any further purification. These CNTs have an average diameter of 128 nm (~40 layers thick) and an average length of 2.5 μm. Detailed length and diameter distribution data are included in Supporting Information (Fig. S1). PLA filaments were purchased from 3D maker world (Cat# 4043D).

Molecular Weight Characterization

Molecular weights of neat PLA and CNT-PLA composites were characterized using gel permeation chromatography (GPC; Waters GPC-1 equipped with 1515 HPLC Pump, Waters 717Plus Autoinjector & Varian Model 380-LC Evaporative Light Scattering Detector) with tetrahydrofuran (THF) from Sigma-Aldrich (Lot# SHBG6390V, ≥99% purity) as the solvent. Approximately 50 mg of samples was dissolved in 20 ml of THF and stored at room temperature for 24 h. To remove CNTs and any impurities, the solutions were then filtered through a 0.45 μm syringe filter before injecting them through the GPC column. The bulk density of neat PLA and CNT-PLA composites was calculated by measuring the weight and volume of the samples.

Optical and Electron Microscopy

Optical microscopy was carried out using Olympus BX50 coupled with a PAXCam CCD camera for capturing images. A single PLA or CNT-PLA pellet was sandwiched between two glass slides and hot pressed at 160°C for 30 s. The hot-pressed films with glass slides were then cooled and observed under the microscope. Scanning electron microscopy (SEM; JEOL 6335 Field Emission SEM) was performed after sputtering a thin layer (3–5 nm) of gold and palladium onto the fractured tensile test coupons to prevent charging. An accelerating voltage of 10 kV was used for capturing all the images.

X-ray Diffraction

For 1D diffraction pattern, CNT-PLA composites were hot pressed into a disc. The peak at 26° with a d-spacing of 3.38 Å corresponds to the interlayer spacing of multiwalled CNTs (Supporting Information, Fig. S2). For 2D diffraction pattern on FDM samples, only one layer was printed to ensure there is sufficient transmitted X-ray signal. The printed sample was mounted on the holder and care was taken to properly align the sample using the built-in CCD camera, such that the incident beam would either hit the raster center or raster intersection as illustrated in Fig. 6a. Diffraction pattern of the transmitted X-ray was collected onto the detector placed at 65 cm from the sample. The faint ring corresponding to a 2θ of 26° forms the diffraction pattern of the CNTs aligned along the road axis. The full width at half maximum (FWHM) of the azimuthal ring integral quantifies the average alignment of CNTs along the road axis and in the load bearing direction. CNT alignment at the raster center and the raster intersection is then compared to help understand the mechanical properties of 3D printed samples.

 DOI 10.1002/pc

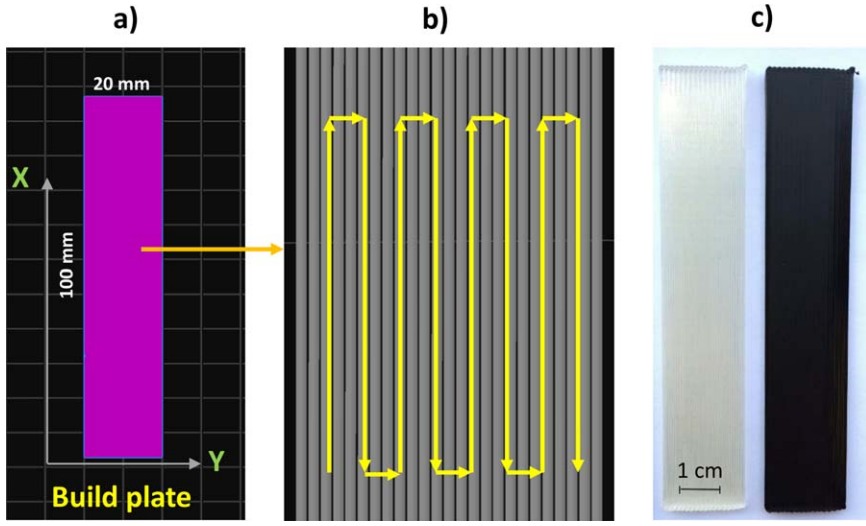

FIG. 1. (a) Computer-aided design (CAD) rendering of a test coupon, (b) Chosen toolpath for printing a test coupon, where the extruded filaments, or "roads," align along the load bearing direction in subsequent mechanical testing. (c) Actual 3D printed 0% CNT-PLA (left) and 5% CNT-PLA (right) test coupons. [Color figure can be viewed at wileyonlinelibrary.com]

Thermogravimetric Analysis (TGA)

TA Instruments TGA Q-500 was used for TGA of the samples after 3D printing. Samples were cut into a small piece weighing about 12 mg for TGA. All the samples were analyzed using air and an arbitrarily chosen temperature ramp rate of 10°C/min. Thermal degradation temperature is taken as the maximum of the first derivative of weight loss with respect to temperature.

Differential Scanning Calorimetry (DSC)

Thermal transitions of the samples before and after 3D printing were analyzed using TA Instruments DSC Q-100. The sample temperature was equilibrated at 0°C for 5 min before increasing to a final temperature of 220°C at a ramp rate of 20°C/min. After reaching 220°C, the sample was held at this temperature for 5 min before ramping down to 0°C at a ramp rate of 20°C/min. %Crystallinity of the samples were calculated using the equation

$$\%\text{Crystallinity} = \frac{\Delta H_f^{obs}}{\Delta H_f^{\circ}} = \frac{\Delta H_m - \Delta H_c}{\Delta H_f^{\circ}} \quad (1)$$

where $\Delta H_m, \Delta H_c$ and ΔH_f^o (= 93.1 J/g) [19] are enthalpy of melting, enthalpy of crystallization and enthalpy of fusion for 100% crystalline PLA, respectively.

3D Printer Feed Filament Preparation

FDM printer in this study uses 1.75 mm (dia.) thermoplastic filaments as the feedstock material. Hydrolysis of PLA accelerates in humid conditions above the glass transition temperature of PLA [20]. To prepare the feed filaments, PLA and CNTs were vacuum dried at room temperature for at least 48 h to minimize hydrolysis of PLA during processing. Different amounts of CNTs were compounded with PLA using a Haake Minilab Twin Screw Extruder (counter rotating screw, 100 rpm, 160°C, 5 min) until the torque reading became constant before extrusion through a circular die. Spin-draw ratio was varied, for samples with different CNT loadings, to keep the diameter of the extruded filament constant. The extruded samples were fed to a filament chopper, pelletized, and dried at room temperature for 48 h. These pellets were then extruded again through a 1.75-mm diameter circular die using the twin screw extruder in continuous mode and wound on an in-house built pick-up roll while maintaining a consistent filament diameter of 1.75 mm ± 0.1 mm. The second extrusion was necessary to produce continuous filaments, as the compounding mode is limited to extruding 4 g of materials at a time. As the thermal history affects the molecular weight and properties, the control PLA sample was prepared following the same extrusion procedure with no CNTs added.

3D Printing Mechanical Test Coupons

Hyrel System 30 3D printer was used in this study. The printer has a build volume of 250 × 200 × 200 mm^3 ($X \times Y \times Z$) and a positional accuracy of 50 × 50 × 20 μm^3 ($X \times Y \times Z$). Rectangular test coupons with dimensions of 100 × 20 × 1.8 mm^3 ($L \times W \times T$) were 3D printed with a layer thickness of 300 μm and 6 layers. A nozzle diameter of 500 μm was used and the set temperatures of the nozzle and build plate were 210 and 50°C, respectively. Test coupons, as shown in Fig. 1, were printed from a Computer-aided design (CAD) file, which was first converted to a stereolithography (.stl) file

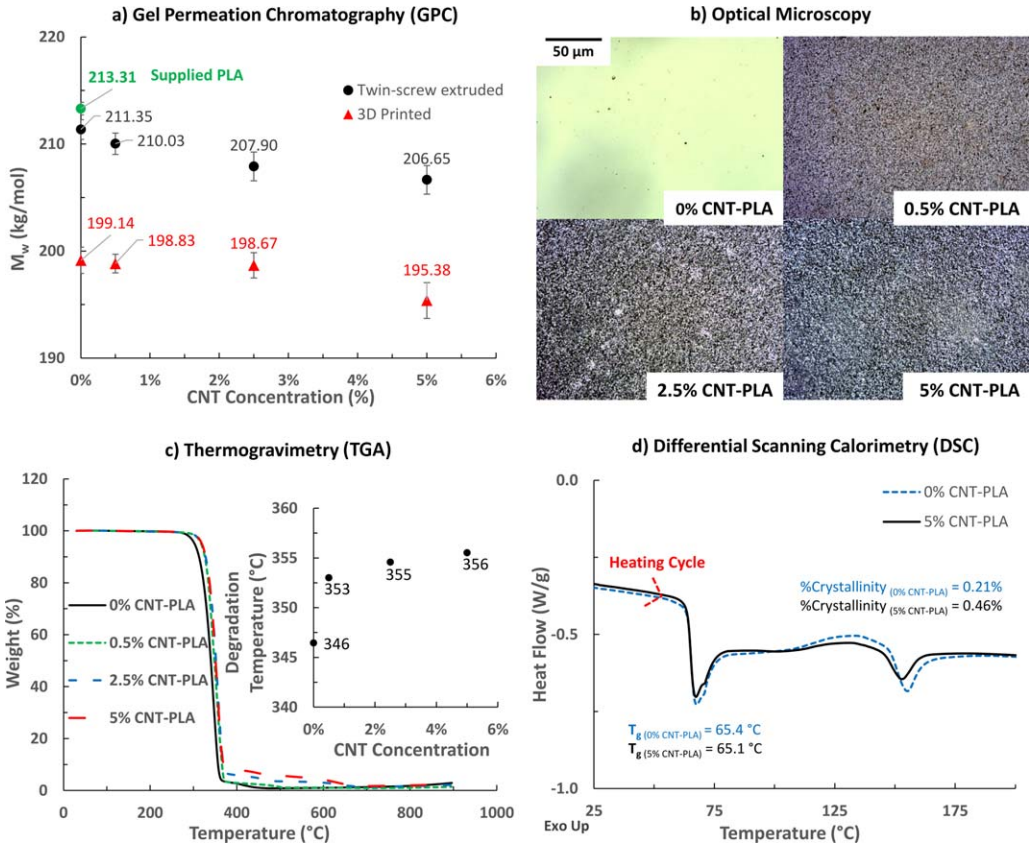

FIG. 2. (a) GPC data for twin screw extruded and CNT-PLA composites 3D printed at 210°C. (b) Optical micrographs of hot pressed composite films showing the difference in optical texture with increasing CNT concentration. Same scale in all micrographs. (c) TGA data of extruded CNT-PLA composites; inset – degradation temperature for corresponding samples in air. (d) First heating cycle of DSC data for 0% CNT-PLA and 5% CNT-PLA sample with %crystallinity. [Color figure can be viewed at wileyonlinelibrary.com]

and further into a g-code using Slic3r®. In this study, the toolpath was chosen such that the extruded filaments, or "roads," aligned along the load bearing direction of the test coupons in subsequent mechanical testing (Fig. 1b).

Mechanical Testing

Mechanical test data were collected using Instron 5869. To protect the coupon from being damaged by the clamps, aluminum plates were glued onto the two ends of the coupon using Loctite E-20HP, a high strength epoxy (McMaster, Cat# 6,430A19). Stress-strain data were recorded to calculate the Young's modulus and tensile strength of the neat PLA and CNT-PLA composites. A constant displacement rate of 1 mm/min was arbitrarily chosen and a minimum of three samples were measured per experimental condition.

Rheology and Sample Preparation

Discs with 25-mm diameter and 1-mm thickness were prepared by compression molding pellets of control and compounded samples at 160°C for 1 min. The cavity of the mold is connected to an overflow channel for capturing any excess material. The mold was sandwiched between steel plates with Kapton® lining to allow easier sample removal. The mold was cooled down to room temperature before the samples were removed. Rheological experiments were carried out on a strain-controlled rheometer (ARES, TA Instruments) using a 25-mm (dia.) parallel plate fixture. The sample was heated to 210°C and squeezed to a gap of 1 mm before excess material was trimmed from the edge. Steady state data were collected at 210°C from a shear rate of 0.1–10 s^{-1}. First data point was measured after a delay of 60 s. For a given shear rate, the apparent viscosity value was averaged over a time period of 60 s.

RESULTS AND DISCUSSION

Molecular Weight and CNT Dispersion

PLA thermally degrades, through oxidation and hydrolysis, during melt processing [7]. Molecular weight and molecular weight distribution have an important impact on the mechanical properties of polymers. In general, the

 DOI 10.1002/pc

higher the molecular weight, the better the mechanical properties. Figure 2a shows the weight average molecular weight of as-supplied PLA and PLA after compounding and 3D printing, respectively. Despite the precautions taken to dry PLA and CNT, PLA degradation was still observed. Molecular weight of PLA decreased slightly from 213.31 to 211.35 kg/mol in the absence of CNT. The molecular weight distribution characterized as the polydispersity index remains the same at 1.3 before and after compounding PLA. The molecular weight of PLA in samples containing CNTs was lower probably due to the residual moisture present in CNTs, which further contributes to hydrolysis. Further decrease in molecular weight was observed after 3D printing, but the difference between samples with and without CNTs is relatively small (<2%).

Figure 2b shows optical micrographs of PLA and CNT-PLA composites with different CNT loadings (0.5, 2.5, and 5%). These samples were prepared by hot pressing a short filament segment into thin films with a thickness of about 20 μm. Although optical microscopy cannot resolve individual CNTs, the global optical texture suggested the presence of CNT aggregates that are larger than the optical diffraction limit (~1 μm). Further, XRD analysis indicated no preferential alignment of CNTs in these samples (Supporting Information Fig. S3). The overlap between CNT aggregates prevented further aggregate size analysis, but no clogging occurred during 3D printing, implying these aggregates were smaller than the nozzle diameter (500 μm) under the flow conditions of 3D printing. However, these CNT aggregates will contribute to local CNT concentration variation and negatively impact the mechanical strength of the printed CNT-PLA composites.

Thermal Degradation and Thermal Transitions

The thermal stability of PLA and CNT-PLA composites was characterized using TGA and the results are shown in Fig. 2c. As a control sample, the "0% CNT-PLA" sample was prepared following the same compounding and extrusion conditions except that no CNT was added. The thermal degradation temperature was recorded as the peak in the first derivative of weight loss with respect to temperature (not shown). The thermal degradation temperature of pristine CNT is 828°C (Supporting Information Fig. S4), whereas that of 0% CNT-PLA is 346°C. The thermal degradation temperature of CNT-PLA composites increased as a function of increasing CNT concentration as shown in Fig. 2c. Similar observations have been previously reported by Wu *et al.* and other research groups [21–24]. CNT has a thermal conductivity close to diamond [25], and the inclusion of CNTs increases the overall thermal conductivity of the CNT composites leading to better heat dissipation and consequently an increase in degradation temperature [24].

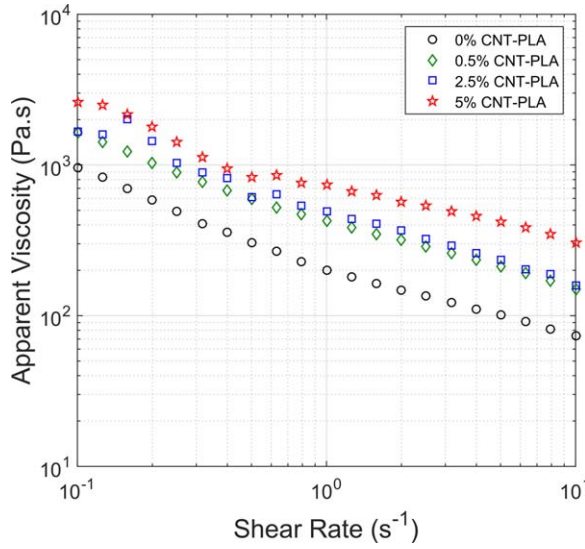

FIG. 3. Apparent viscosity as a function of shear rate for different weight concentrations of CNT in PLA at 210°C. A 25-mm parallel plate fixture was used. The reported shear rate corresponds to the maximum shear rate at the edge of the parallel plates. [Color figure can be viewed at wileyonlinelibrary.com]

The thermal transitions of neat PLA and CNT-PLA composites were studied using DSC. Figure 2**d** shows the thermal transitions from the first heating cycle of 5% CNT-PLA, sample with highest CNT loading. No significant difference was observed in the glass transition temperature between neat PLA and CNT-PLA composites, ranging between 65 and 66°C. Further, the degree of crystallinity was calculated using the enthalpy of crystallization and enthalpy of melting (*Eq. 1*) and was observed to be ≤1.2% in all cases. Full DSC data are included in Supporting Information (**Table SI**). The inclusion of CNT has negligible effect on the degree of crystallinity of the PLA used in this study. This is probably due to the relatively fast cooling rate involved in 3D printing as the diameter of the printed roads is rather small (<1 mm). Prior studies by Xu *et al.* and Shieh *et al.* suggested that a CNT loading <10 wt% did not induce PLA crystallization at a cooling rate of 10°C/min or higher [26, 27]. The low degree of PLA crystallinity is advantageous for 3D printing because higher crystallinity is associated with higher shrinkage and potential warpage of the printed parts [28].

Rheology and Flow Rate Calibration

Figure 3 shows the apparent shear viscosity as a function of shear rate for different CNT loadings at 210°C. Inclusion of CNT in PLA increased the apparent shear viscosity. The degree of viscosity increase depends on CNT orientation and state of aggregation [29]. The CNTs used in this study has an aspect ratio (λ) of 19.5 (length to diameter ratio) and the crossover from dilute to semi-dilute behavior is estimated to be at a concentration of 9.4% (w/w) ($=24\rho_{CNT}/\rho_{PLA}\lambda^2$), assuming a CNT density (ρ_{CNT}) of 1.8 g/cm^3 and PLA density (ρ_{PLA}) of 1.2 g/cm^3

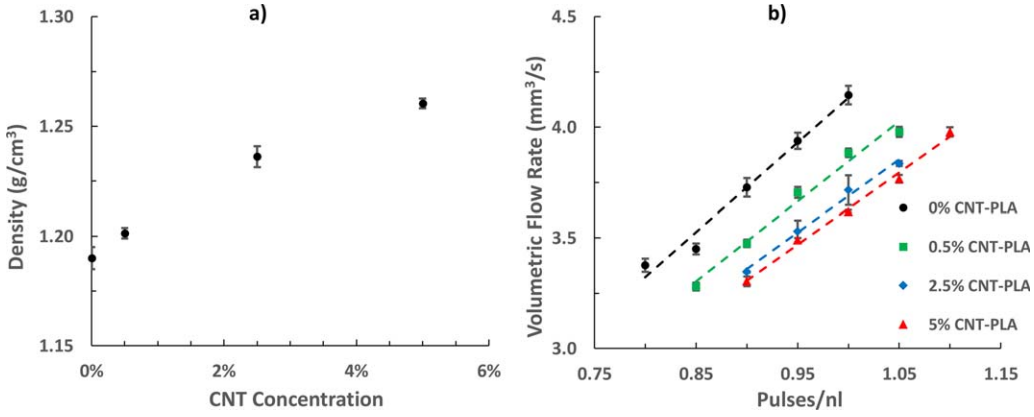

FIG. 4. (a) Measured density of PLA and CNT-PLA samples based on a minimum of ten samples for each data point. (b) Volumetric flow rate (mm^3/s) as a function of "pulses/nl". [Color figure can be viewed at wileyonlinelibrary.com]

[30]. Despite the relatively high loading, 5% (w/w) CNT in PLA, if individually dispersed, remains within the dilute regime, where there is no CNT-CNT interactions and the viscosity enhancement effect is caused by hydrodynamic interactions [31]. However, this simple analysis does not account for the presence of CNT aggregates.

A power-law fluid model ($\eta_s = K\dot{\gamma}^{n-1}$) was fitted to the steady shear viscosity data of the 0% CNT-PLA sample, giving $K = 230.05$ Pa.s$^{0.49}$ and $n = 0.49$. Shear rate is a function of the radial position within the liquefier. It is zero at the center and highest at the wall. If no slip at the wall is assumed, the wall shear rate for a power law fluid ($\dot{\gamma}_w$) can be calculated using the equation below [32]:

$$\dot{\gamma}_w = \left(3 + \frac{1}{n}\right)\frac{Q}{\pi r^3} \tag{2}$$

where Q is the volumetric flow rate, r is the radius of the liquefier, and n is the power law coefficient. The wall shear rate in the liquefier is estimated to be 0.74 s^{-1} for $Q = 3.7$ mm^3/s, $r = 2$ mm, and $n = 0.49$.

During the 3D printing process, the hydrodynamic forces may break up the aggregates and align the CNT along the extrusion direction. Peclet number (Pe) compares the hydrodynamic forces versus the thermal motions, which lead to randomization of CNT orientation. It is defined as:

$$Pe = \frac{\dot{\gamma}}{D_r} \tag{3}$$

where $\dot{\gamma}$ is the shear rate and D_r is the rotary diffusivity of CNT and is further calculated using the following equation [30]:

$$D_r = \frac{3k_BT(\ln(l/d) - 0.8)}{\pi\eta_s l^3} \tag{4}$$

where k_B is the Boltzman constant, T is the temperature, η_s is the viscosity of the suspending medium, and l and d are the length and diameter of the CNTs used, respectively.

The viscosity of the suspending medium (η_s) at a shear rate of 0.74 s^{-1} is calculated to be 268 Pa·s using the power law model. Based on *Eq. 4*, D_r is calculated to be 3.34×10^{-6} s^{-1}, giving a Peclet number on the order of 2.21×10^5 at the wall. Pe $\gg$ 1 suggests hydrodynamic forces dominate random thermal motions, aligning CNTs in the flow direction. This was later confirmed experimentally in **Section "CNT orientation**." However, this relatively simple order-of-magnitude analysis does not account for the aggregates that are initially present, wall slippage, or flow-induced CNT aggregation, which will reduce the degree of CNT alignment. Further, in the actual print nozzle geometry (Supporting Information Fig. S5), the nozzle is tapered. The converging flow further leads to extensional deformation, which aligns the CNTs more effectively than simple shear flows because of the absence of a rotation component [33–35].

In a FDM printer, the solid feed filament is driven into the liquefier using a pair of pinch rollers. Further, the printing flow rate is controlled by a set parameter called "pulses/nl", which is related to the rotation speed of the pinch rollers. The relation between printing flow rate and this parameter is not readily available. As a result, flow rate calibration was carried out. For a given pulses/nl value, the actual mass flow rate was calculated by weighing the printed samples and measuring the time required to print one layer multiplied by the total number of layers printed. Multiplication is performed to exclude the idle time in between printing different layers. The calculated mass flow rate was then divided by the measured density (Fig. 4a) to give the volumetric flow rate. For a given pulses/nl value, the volumetric flow rate decreases with increasing CNT loading, as shown in Fig. 4b. This trend may be explained by the increase in viscosity due to CNT inclusion. First, inclusion of CNT increases the viscosity, which in turn decreases the volumetric flow rate for a fixed pressure drop and geometry. Second, if the viscosity is too high, the friction may not be able to hold the

 DOI 10.1002/pc

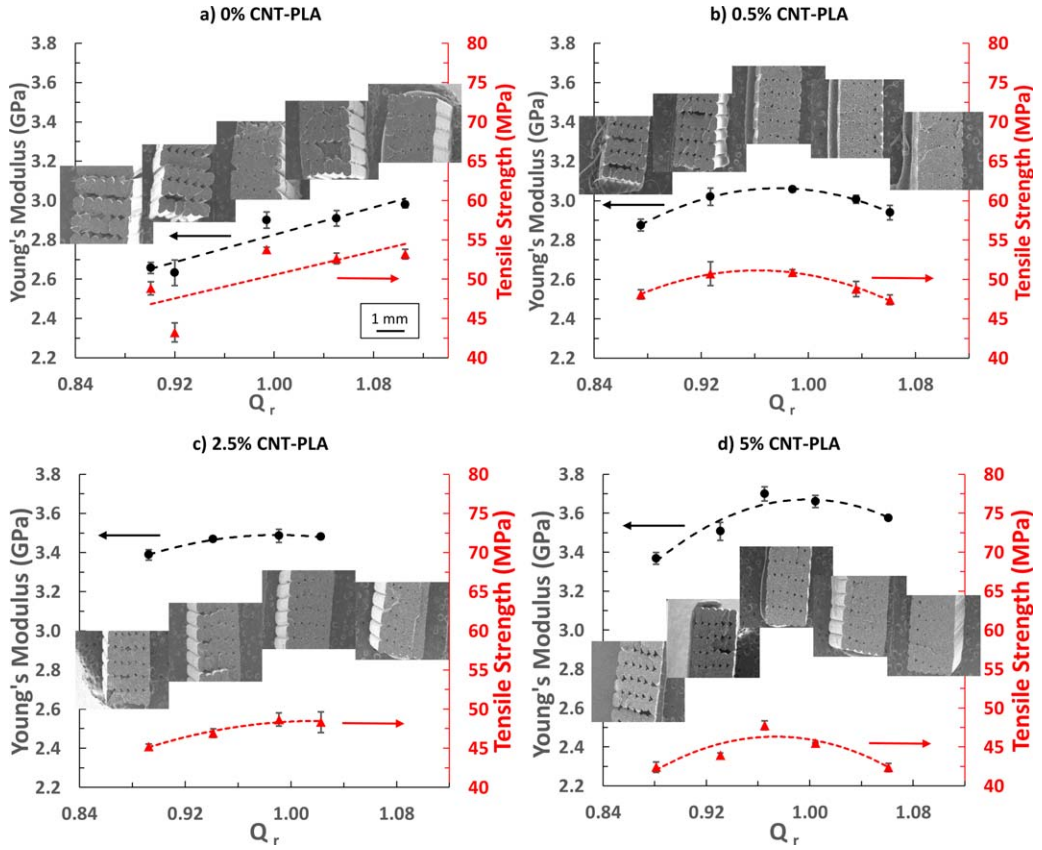

FIG. 5. Young's modulus, tensile strength, and scanning electron micrographs of the fractured surface as a function of dimensionless volumetric flow rate (Qr) for (a) 0% CNT-PLA, (b) 0.5% CNT-PLA, (c) 2.5% CNT-PLA, and (d) 5% CNT-PLA, respectively. Amount of void fraction decreases as a function of increasing Qr. Same scale as shown in (d) applies to all SEM images. [Color figure can be viewed at wileyonlinelibrary.com]

filament in place, leading to a slip at the roller-filament interface and a reduction in actual filament displacement and volumetric flow rate [36].

Mechanical Properties

Effect of Printing Flow Rate. The width of the extrudate depends on the interplay between printing flow rate, velocity of the print nozzle relative to the build plate, and the gap between nozzle and the build plate [18]. For a given gap size and relative nozzle velocity, a higher volumetric flow rate will lead to wider extrudate. Likewise, a smaller gap or a lower relative nozzle velocity will also result in extrudate overfilling the gap. In this study, we define a dimensionless volumetric flow rate (Q_r) taking into considerations the relative nozzle velocity and cross-sectional area of the extrudate for a fixed gap and nozzle diameter:

$$Q_r = \frac{Q_{actual}}{Q_{ideal}} = \frac{Q_{actual}}{d_{nozzle} h v} \quad (5)$$

where Q_{actual} is the actual volumetric flow rate calculated from calibration curves (Fig. 4), Q_{ideal} is the ideal volumetric flow rate required to completely fill a given gap between the nozzle and the build plate at a given relative velocity of the print head, d_{nozzle} is the print nozzle diameter (0.5 mm), h is the gap between the nozzle and the build plate (0.3 mm), and v is the relative velocity of the print head (25 mm/s). $Q_r > 1$ indicates "over-flow" and $Q_r < 1$ indicates "under-flow."

Figure 5 shows the Young's modulus, tensile strength, and corresponding electron micrographs of the fractured surface as a function of Q_r for different CNT loadings. In FDM printing, laminate-like mesostructures are formed as printed roads are partially bonded and fused together. Like laminates [37], the overall mechanical properties of FDM parts depend on the bonding between different layers (ply), the void density, and the strength of individual extrudate. The latter further depends on the matrix material, filler concentration, filler dispersion quality, filler orientation, and the stress transfer between the matrix and filler. The bond formation between printed roads and the resulting bond strength are strongly influenced by these process parameters as well as heat transfer. As a road is freshly printed, the temperature is initially above the glass transition temperature, but decreases due to heat loss to the surrounding via conduction, convection, and radiation. As an adjacent road is laid down, the

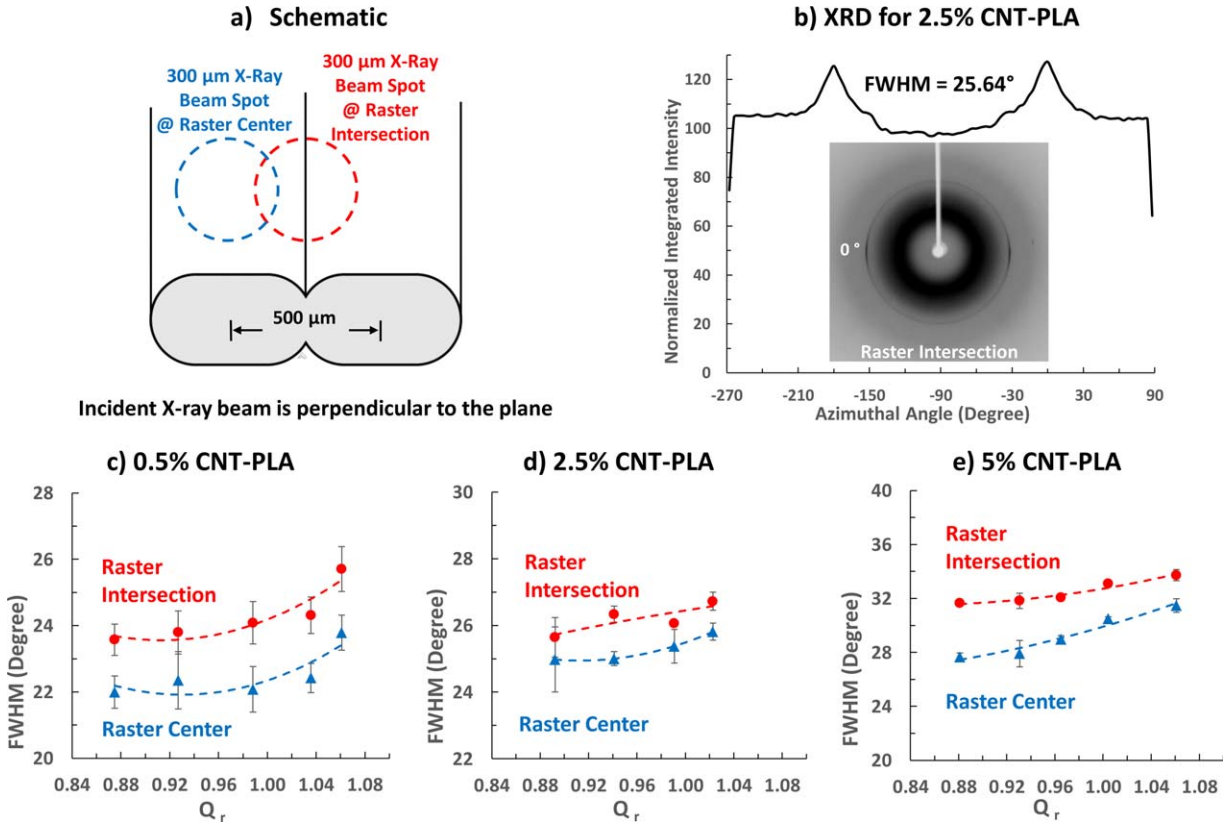

FIG. 6. (a) Schematic diagram shows the two different locations of X-ray beam spot for collecting XRD data. (b) XRD pattern for 2.5% CNT-PLA measured at the raster intersection. FWHM of: (c) 0.5% CNT-PLA, (d) 2.5% CNT-PLA, and (e) 5% CNT-PLA as a function of Qr. The error bar represents the standard deviation of at least three samples. [Color figure can be viewed at wileyonlinelibrary.com]

temperature of previously printed road increases again and a "neck" is formed between two roads. The bond quality depends on the amount of residual heat available to enable the molecular diffusion and randomization of polymer chains at the road-road interface. Neck growth slows down almost instantaneously as the roads rapidly cool down after extrusion. The mesostructures of the printed CNT-PLA strongly depend on dimensionless volumetric flow rate, Q_r. For a fixed extrudate-to-extrudate distance, $Q_r > 1$ leads to a wider neck, whereas $Q_r < 1$ results in a narrower neck or lack of bonding between the roads as illustrated in Fig. 7.

As shown in Fig. 5, in the absence of CNT, the Young's modulus and tensile strength of PLA samples increase as a function of increasing Q_r. This is attributed to the reduction in void fraction and better bonding between individual PLA roads. In the case of CNT-PLA samples, the highest Young's modulus and tensile strength were observed at Q_r close to 1. Like the neat PLA case, increasing the volumetric flow rate for underfilled samples ($Q_r < 1$) reduces the void fraction between roads and increases the stress transfer between individual roads under tension. Theoretically, as the volumetric flow rate is increased, the shear rate within the liquefier should also increase, leading to a higher degree of CNT alignment and consequently higher modulus. However, the opposite trend was observed. We hypothesize that this is related to CNT alignment and overfilling ($Q_r > 1$) randomizes CNT orientation. To examine this hypothesis, XRD analysis was carried out to evaluate the CNT alignment both within and in between the printed roads.

CNT Orientation. XRD was carried out to quantify the degree of CNT alignment both within a printed road and at the intersection between the roads as illustrated in Fig. 6a. 1D diffraction pattern (Supporting Information Fig. S2) suggests the 2θ peak at 26° corresponds to a d-spacing of 3.38 Å [38], originating from the interlayer spacing between the walls of multiwalled CNTs. The faint ring in the 2D diffraction pattern (Fig. 6b), where 2θ is ~26°, is used to quantify the CNT alignment by calculating the FWHM of the azimuthal ring integral. In the case of 2.5% CNT-PLA, the average FWHM from two peaks at 0° and 180° is 25.64°, indicating that the CNTs are, on average, aligned at 25.64° from the load bearing direction, which is the same as the road axis. Similar data were collected from one-layer thick CNT-PLA composites for different CNT loadings and Q_r. A minimum of three samples were measured for each case, and the average FWHM values are shown in Fig. 6. SEM images for

DOI 10.1002/pc

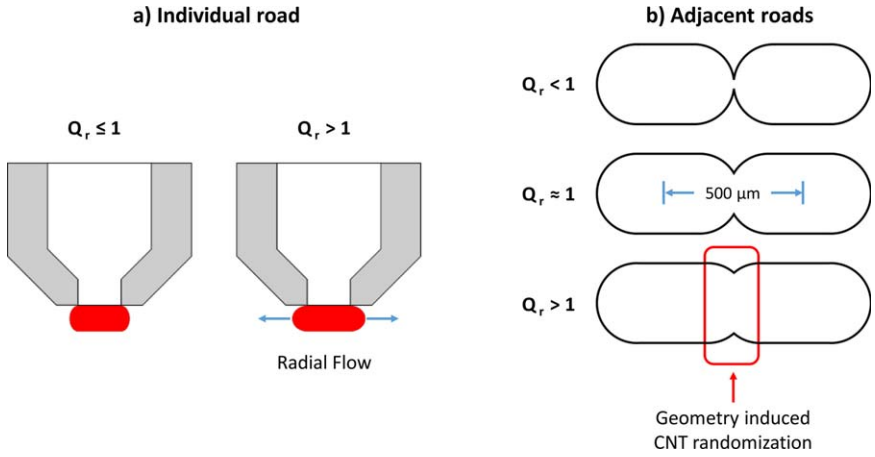

FIG. 7. Schematic diagrams of hypothesized factors leading to CNT misalignment during 3D printing: (a) radial flow as the material overfills the gap and (b) geometry-based fusion between adjacent roads. [Color figure can be viewed at wileyonlinelibrary.com]

CNT-PLA composites were also collected, confirming the preferential alignment of CNTs along the road axis (Supporting Information Fig. S6). However, SEM data were not used for quantifying the CNT orientation as the vibratome step during sample preparation may have modified the aggregation state and/or alignment of CNTs [39].

As shown in Fig. 6c, FWHM increases as a function of increasing Q_r for the 0.5% CNT-PLA samples, implying the degree of CNT alignment decreases as a function of increasing Q_r. A similar trend is also observed for the 2.5 and 5% CNT-PLA samples (Fig. 6d and e). This trend is counter-intuitive because a higher Q_r will lead to a higher wall shear rate and thus higher degree of alignment. However, this experimental observation may be explained by a combination of flow and geometry-induced effects, as illustrated in Fig. 7a and b. First, if the gap and the relative velocity between the print nozzle and the build plate are fixed, more material flows out of the nozzle with increasing Q_r, which results in radial flow in the lateral direction (Fig. 7a). This radial flow results in less degree of CNT alignment along the printing direction. Second, CNT alignment will likely decrease as two adjacent extrudates fuse together (Fig. 7b). This geometry-induced misalignment becomes more significant as Q_r increases, especially for $Q_r \geq 1$.

Further, Fig. 6c–e show that CNTs are less aligned at the intersection compared to that at the center. Although a higher degree of CNT alignment is expected at the intersections due to the higher shear rates close to the wall within the liquefier, this was not observed experimentally. This may be explained by die swelling as well as the combined flow and geometry-induced effects, to which the center of the extrudates is less susceptible. A similar trend has been reported in a FDM simulation study carried out by Heller *et al*. The higher degree of fiber alignment at the core of the extrudate relative to the wall is attributed to a convergence zone of the nozzle—similar to the one used in this experimental study. For a given volumetric flow rate, the flow velocity increases as the cross-sectional area decreases. The increase in flow velocity leads to extensional deformations, which further align the fibers at the core [35].

Effect of CNT Concentration and Micromechanical Models

Figure 8 shows the Young's modulus of the FDM-printed coupons increases as a function of increasing CNT concentration for $Q_r \approx 1$. Inclusion of CNT with higher modulus is expected to increase the overall modulus. However, the dispersion quality of CNTs and CNT alignment also vary depending on the CNT loading. The higher the CNT loading, the less degree of CNT alignment along the road axis. This may be explained by the higher tendency for CNTs to aggregate at higher concentration [29]. Additionally, CNT aggregates also lead to fluctuations in local CNT concentration, which further results in stress concentration and weaker parts.

Experimental data are further compared against three commonly used micromechanical models, namely rule of mixtures (RoM), Halpin-Tsai, and modified RoM. Experimentally, the modulus does not increase linearly as predicted by the RoM or the Halpin-Tsai model.

First, in the RoM model, the composite modulus is calculated using the following equation:

$$E_c = E_m(1 - V_f) + E_f V_f \tag{6}$$

E_c, E_m, and E_f are the modulus of the composite, matrix, and filler, respectively, and V_f is the filler volume fraction. The CNT modulus is assumed to be 500 GPa, which is an average value based on a range from 20 to 800 GPa reported for CNTs with a similar diameter [40].

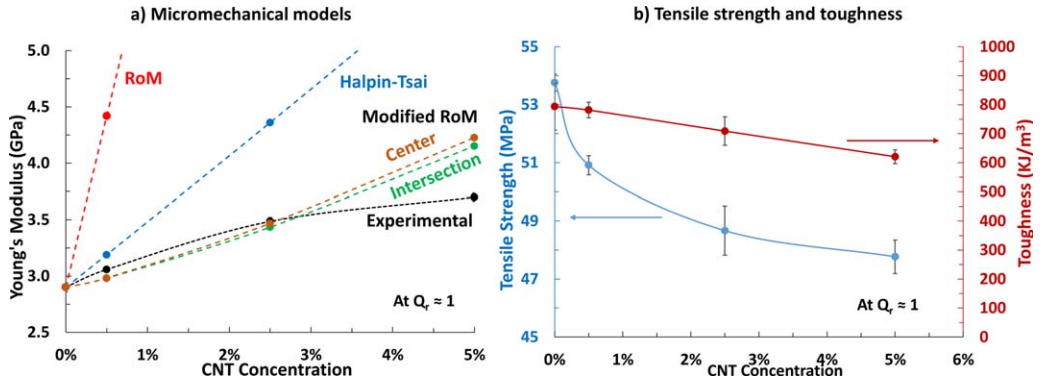

FIG. 8. (a) Effect of CNT concentration on Young's modulus of FDM parts at Qr = 1. Three micromechanical models, namely, RoM, Halpin-Tsai model, and modified RoM, were used. For the modified RoM model fit, the upper and lower bounds were calculated from XRD data measured at the raster center and raster intersection, respectively. The error bars represent standard deviation of at least three measurements. (b) Tensile strength and toughness of CNT-PLA composites at Qr = 1. A minimum of three samples were tested for every data point to calculate the standard deviation. [Color figure can be viewed at wileyonlinelibrary.com]

The RoM model assumes: (i) perfect bonding exists between fillers and matrix, (ii) a longitudinal load produces equal strain in fillers and matrix, and (iii) the fillers are continuous and are in parallel. These assumptions are not met for the CNT-PLA system and this may explain the large discrepancy observed.

Second, Halpin-Tsai model for discontinuous fiber composites is considered where the longitudinal modulus ($E_{//}$) of the composite is calculated using the equation below [41].

$$E_{//}=E_{\mathrm{m}}\left[\frac{1+2\frac{l}{d}\eta_{//}V_{\mathrm{f}}}{1-\eta_{//}V_{\mathrm{f}}}\right] \tag{7}$$

where

$$\text{Longitudinal efficiency factor } =\eta_{//}=\left[\frac{\left(\frac{E_{\mathrm{f}}}{E_{\mathrm{m}}}\right)-1}{\left(\frac{E_{\mathrm{f}}}{E_{\mathrm{m}}}\right)+2\left(\frac{l}{d}\right)}\right] \tag{8}$$

For continuous fibers, it is assumed that the stress and strain are uniform in the longitudinal direction. However, this assumption is likely to fail in the case of discontinuous fibers. As short stiff fibers are embedded within a more flexible matrix, shear stresses and strains are maximum at the fiber ends. Short fibers carry load less effectively compared with long fibers and hence have less reinforcement efficiency, which the Halpin-Tsai model fails to capture.

Third, a modified RoM, as described by Coleman *et al*., is used [42]. This model incorporates into the RoM model a length correction factor (η_{L}) based on the shear lag theory developed by Cox [43] and an orientation correction factor known as the Krenchel orientation correction (η_{o}). These correction factors accounts for the loss of efficiency when fibers are neither continuous nor unidirectional. Composite modulus using the modified RoM model is given by:

$$E_{\mathrm{c}}=E_{\mathrm{m}}(1-V_{\mathrm{f}})+\eta_{\mathrm{L}}\eta_{\mathrm{o}}E_{\mathrm{f}}V_{\mathrm{f}} \tag{9}$$

where,

$$\eta_{\mathrm{L}}=\left(1-\frac{\tan h\left(\frac{\beta l}{d}\right)}{\left(\frac{\beta l}{d}\right)}\right) \tag{10}$$

$$\beta=\sqrt{\frac{-3E_{\mathrm{m}}}{2E_{\mathrm{f}}\ln V_{\mathrm{f}}}} \tag{11}$$

and

$$\eta_{\mathrm{o}}=\frac{\sum_{n} a_{\mathrm{fn}}\cos^4\Phi_n}{\sum_{n} a_{\mathrm{fn}}} \tag{12}$$

β is a measure of stress build up at the fiber ends [43]. Mathematically, the value of the length correction factor

TABLE 1. A comparison between dE/dV$_{\mathrm{f}}$ values for composites prepared by different processing methods.

Processing method	dE/dV$_{\mathrm{f}}$	Remarks	Reference
3D printing	51.6	Melt compounded	This study
Solid-state drawing	30.0	Drawn (draw ratio = 1)	Mai *et al*. 45
Injection molding	1.1–2.6	Melt compounded	Desa *et al*. 46, 47
Compression molding	83.3–158.3	Solution mixed (functionalized CNTs)	Kim *et al*. 48

The density of CNTs was assumed to be 1.8 g/cm^3 for all calculations.

DOI 10.1002/pc

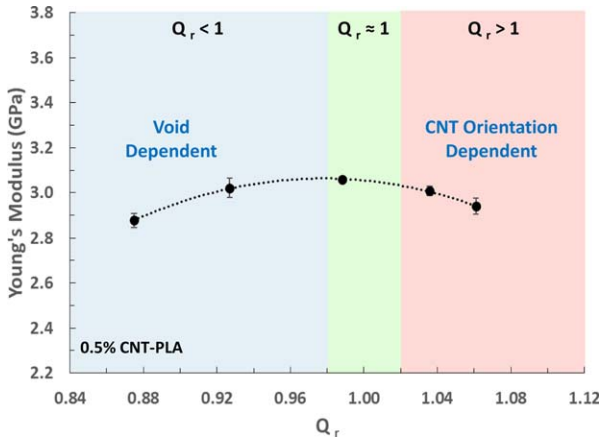

FIG. 9. Effect of printing flow rate on the Young's modulus of 3D printed CNT-PLA composites using 0.5% CNT-PLA as an example. For $Qr < 1$, increasing Qr reduces void fraction and increases modulus, whereas for $Qr > 1$, increasing Qr leads to flow- and geometry-induced CNT misalignment as illustrated in Fig. 7. [Color figure can be viewed at wileyonlinelibrary.com]

(η_L) approaches 1 as the aspect ratio (l/*d*) increases to infinity. Krenchel orientation factor (η_o) is the fraction of fibers (a_{fn}) aligned at an angle Φ with respect to the load bearing direction (see Supporting Information for calculation, *Eq.* **S1**). This information was extracted from XRD data at the raster center and raster intersection, respectively, and used to calculate the modulus of the composite.

All micromechanical models predict that Young's modulus increases with increasing CNT concentration, as shown in Fig. 8a. The modified RoM model, which also considers the CNT orientation, predicts the experimental trend better compared with the RoM and Halpin-Tsai models. The discrepancy between the experimental data and modified RoM predictions at 5% CNT loading is attributed to the poor dispersion and/or poor stress transfer between the CNTs and PLA matrix. Lastly, at low loadings, the initial change in Young's modulus with respect to the change in CNT volume fraction, or dE/dV_f, may be used to compare different experimental results [42, 44]. In this study, an initial slope (dE/dV_f) of 51.6 was calculated. This value is comparable with CNT-PLA composite samples prepared using methods such as compression molding, injection molding, and solid-state drawing, as summarized in Table 1. However, as shown in Fig. 8b, both tensile strength and toughness of the composites decrease with increasing CNT concentration (for $Q_r \approx 1$). The tensile strength and toughness decreased by 11 and 22%, respectively, at 5% CNT loading relative to neat PLA.

CONCLUSIONS

In summary, this study explored the 3D printing of CNT-PLA composites using an extrusion-based FDM method. Feedstock filaments for the FDM 3D printer were prepared by compounding PLA at different CNT loadings, namely, 0.5, 2.5, and 5% by weight. The weight average molecular weight, thermal degradation temperature, and thermal transitions of the 3D printing feedstock materials were characterized before and after compounding and after 3D printing. The effects of volumetric flow rate and CNT concentration on the microstructure and subsequent mechanical properties of 3D printed test coupons were investigated. The actual printing flow rate during 3D printing was calibrated. A dimensionless volumetric flow rate, Q_r, was further defined. Q_r is essentially a "gap-filling" index and is based on the printing flow rate as well as the gap size and the relative velocity between the print nozzle and the build plate. $Q_r < 1$ indicates under-flow, whereas $Q_r > 1$ indicates over-flow. Q_r was found to be a critical parameter in understanding the microstructure and subsequent mechanical properties of FDM parts (as shown in Fig. 9). For $Q_r < 1$, increasing Q_r reduced the void fraction in FDM parts and thus increased the Young's modulus. However, in the case of CNT-PLA composites, the Young's modulus decreased as a function of increasing Q_r, for $Q_r > 1$. XRD data further revealed the higher the Q_r, the lower degree of CNT alignment along the road axis, which is the same as the load bearing direction in mechanical testing. We hypothesized that this is caused by radial flow and fusion between adjacent roads. Additionally, the difference between CNT alignment at the intersection between printed roads and within individual roads suggested the importance of a convergence zone within the printer chamber, consistent with a recent FDM simulation study [35]. Lastly, inclusion of 5% CNTs (by weight) increased the Young's modulus of the FDM parts by 30%, but the tensile strength and toughness decreased by 11 and 22%, respectively. The effects of CNT concentration and orientation on Young's modulus were studied and compared against three micromechanical models.

ACKNOWLEDGMENTS

The authors would like to acknowledge Prof. Mu-Ping Nieh (University of Connecticut) for his valuable guidance with X-ray diffraction.

Contract grant sponsor: GE graduate fellowship.

REFERENCES

1. W. Wu, A. DeConinck, and J.A. Lewis, *Adv. Mater.*, **23**, 178 (2011).
2. S.Z. Guo, X. Yang, M.C. Heuzey, and D. Therriault, *Nanoscale*, **7**, 6451 (2015).
3. M. Hajihosseini, J. Faradmal, and A.S. Pashaki, *Iran J. Public Health*, **44**, 1677 (2015).
4. R.W. Gray IV, D.G. Baird, and J.H. Bohn, *Rapid Prototyp. J.*, **4**, 14 (1998).
5. J.M. Gardner, G. Sauti, J.W. Kim, R.J. Cano, R.A. Wincheski, C.J. Stelter, B.W. Grimsley, D.C. Working, and E.J. Siochi, *Addit. Manuf.*, **12**, 38 (2016).

6. S. Dul, L. Fambri, and A. Pegoretti, *Compos. A*, **85**, 181 (2016).
7. T. Maharana, B. Mohanty, and Y.S. Negi, *Prog. Polym. Sci*., **34**, 99 (2009).
8. T. Tábi, I.E. Sajó, F. Szabó, A.S. Luyt, and J.G. Kovács, *Express Polym. Lett*., **4**, 659 (2010).
9. H.J. Qi, K.B.K. Teo, K.K.S. Lau, M.C. Boyce, W.I. Milne, J. Robertson, and K.K. Gleason, *J. Mech. Phys. Solids*, **51**, 2213 (2003).
10. P. Kim, L. Shi, A. Majumdar, and P. McEuen, *Phys. Rev. Lett*., **87**, 215502 (2001).
11. E. Bekyarova, M.E. Itkis, N. Cabrera, B. Zhao, A. Yu, J. Gao, and R.C. Haddon, *J. Am. Chem. Soc*., **127**, 5990 (2005).
12. R. Matsuzaki, M. Ueda, M. Namiki, T.K. Jeong, H. Asahara, K. Horiguchi, T. Nakamura, A. Todoroki, and Y. Hirano, *Sci. Rep*., **6**, 23058 (2016).
13. N. Li, Y. Li, and S. Liu, *J. Mater. Process. Technol*., **238**, 218 (2016).
14. H.L. Tekinalp, V. Kunc, G.M. Velez-Garcia, C.E. Duty, L.J. Love, A.K. Naskar, C.A. Blue, and S. Ozcan, *Compos. Sci. Technol*., **105**, 144 (2014).
15. M.L. Shofner, K. Lozano, F.J. Rodríguez-Macías, and E.V. Barrera, *J. Appl. Polym. Sci*., **89**, 3081 (2003).
16. B.G. Compton, and J.A. Lewis, *Adv. Mater*., **26**, 5930 (2014).
17. O. Rishi, Thesis. Rochester Institute of Technology, Feed Rate Effects In Freeform Filament Extrusion (2013).
18. O.S. Carneiro, A.F. Silva, and R. Gomes, *Mater. Des*., **83**, 768 (2015).
19. C.S. Lovell, J.M. Fitz-Gerald, and C. Park, *J. Polym. Sci. Part B: Polym. Phys*., **49**, 1555 (2011).
20. T. Villmow, P. Pötschke, S. Pegel, L. Häussler, and B. Kretzschmar, *Polymer*, **49**, 3500 (2008).
21. B.B. Marosfoi, A. Szabó, G. Marosi, D. Tabuani, G. Camino, and S. Pagliari, *J. Therm. Anal. Calorim*., **86**, 669 (2006).
22. G. Gorrasi, M. Sarno, A. Di Bartolomeo, D. Sannino, P. Ciambelli, and V. Vittoria, *J. Polym. Sci. Part B: Polym. Phys*., **45**, 597 (2007).
23. H.S. Kim, B. Hyun Park, J.S. Yoon, and H.J. Jin, *Eur. Polym. J*., **43**, 1729 (2007).
24. D. Wu, L. Wu, M. Zhang, and Y. Zhao, *Polym. Degrad. Stab*., **93**, 1577 (2008).
25. A.E. Aliev, M.H. Lima, E.M. Silverman, and R.H. Baughman, *Nanotechnology*, **21**, 35709 (2010).
26. H.S. Xu, X.J. Dai, P.R. Lamb, and Z.M. Li, *J. Polym. Sci. Part B: Polym. Phys*., **47**, 2341 (2009).
27. Y.T. Shieh, and G.L. Liu, *J. Polym. Sci. Part B: Polym. Phys*., **45**, 1870 (2007).
28. S.H. Kochesfahani, Improving PLA-based Material for FDM 3D-Printers Using Minerals, *SPE Antec*, 1598 (2016).
29. A.W.K. Ma, F. Chinesta, A. Ammar, and M.R. Mackley, *J. Rheol*., **52**, 1311 (2008).
30. R. G. Larson, The Structure and Rheology of Complex Fluids, Oxford University Press, USA (1999).
31. J. Mewis and N. J. Wagner, Colloidal Suspension Rheology, Cambridge University Press, New York (2012).
32. C. W. Macosko, Rheology: Principles, measurements, and applications, Wiley-VCH, USA (1994).
33. A.W.K. Ma, F. Chinesta, T. Tuladhar, and M.R. Mackley, *Rheol. Acta*, **47**, 447 (2008).
34. G.B. Jeffery, *Proc. R. Soc. London Ser. A*, **102**, (1922).
35. B.P. Heller, D.E. Smith, and D.A. Jack, *Addit. Manuf*., **12**, 252 (2016).
36. B. N. Turner, R. Strong, and S. A. Gold, *Rapid Prototyp. J*., **20**, 192 (2014).
37. P. K. Mallick, Fiber-reinforced composites: Materials, manufacturing, and design; CRC Press, USA (2008).
38. A. Cao, C. Xu, J. Liang, D. Wu, and B. Wei, *Chem. Phys. Lett*., **344**, 13 (2001).
39. P.M. Ajayan, O. Stephan, C. Colliex, and D. Trauth, *Science*, **265**, 1212 (1994).
40. D. Qian, E.C. Dickey, R. Andrews, and T. Rantell, *Appl. Phys. Lett*., **76**, 2868 (2000).
41. D.F. O'Regan, M. Akay, and B. Meenan, *Compos. Sci. Technol*., **59**, 419 (1999).
42. J.N. Coleman, U. Khan, W.J. Blau, and Y.K. Gun'ko, *Carbon*, **44**, 1624 (2006).
43. H.L. Cox, *Br. J. Appl. Phys*., **3**, 72 (1952).
44. J.N. Coleman, U. Khan, and Y.K. Gun'ko, *Adv. Mater*., **18**, 689 (2006).
45. F. Mai, H. Deng, W. Tu, S. Chankajorn, Q. Fu, E. Bilotti, and T. Peijs, *Macromol. Mater. Eng*., **12**, 1257 (2015).
46. M.S.Z. Mat Desa, A. Hassan, A. Arsad, R. Arjmandi, and N.N.B. Mohammad, *J. Appl. Polym. Sci*., **133**, 44344 (2016).
47. M.S.Z. Mat Desa, A. Hassan, A. Arsad, and N.N.B. Mohammad, *Mater. Res. Innov*., **18**, 14 (2014).
48. H.S. Kim, Y.S. Chae, B.H. Park, J.S. Yoon, M. Kang, and H.J. Jin, *Curr. Appl. Phys*., **8**, 803 (2008).

 DOI 10.1002/pc